AGU PUBLICATIONS

Geophysical Research Letters

RESEARCH LETTER
10.1002/2014GL061677

Key Points:
- Steady-state Birkeland currents are present at Mercury
- The currents are 100 times weaker than at Earth and of only Region 1 polarity
- The currents close through the interior of the planet

Correspondence to:
B. J. Anderson,
brian.anderson@jhuapl.edu

Citation:
Anderson, B. J., C. L. Johnson, H. Korth, J. A. Slavin, R. M. Winslow, R. J. Phillips, R. L. McNutt Jr., and S. C. Solomon (2014), Steady-state field-aligned currents at Mercury, *Geophys. Res. Lett.*, *41*, 7444–7452, doi:10.1002/2014GL061677.

Received 26 AUG 2014
Accepted 2 OCT 2014
Accepted article online 7 OCT 2014
Published online 6 NOV 2014

Steady-state field-aligned currents at Mercury

Brian J. Anderson[1], Catherine L. Johnson[2,3], Haje Korth[1], James A. Slavin[4], Reka M. Winslow[2], Roger J. Phillips[5], Ralph L. McNutt Jr.[1], and Sean C. Solomon[6,7]

[1]The Johns Hopkins University Applied Physics Laboratory, Laurel, Maryland, USA, [2]Department of Earth, Ocean, and Atmospheric Sciences, University of British Columbia, Vancouver, British Columbia, Canada, [3]Planetary Science Institute, Tucson, Arizona, USA, [4]Department of Atmospheric, Oceanic and Space Sciences, University of Michigan, Ann Arbor, Michigan, USA, [5]Southwest Research Institute, Boulder, Colorado, USA, [6]Lamont-Doherty Earth Observatory, Columbia University, Palisades, New York, USA, [7]Department of Terrestrial Magnetism, Carnegie Institution of Washington, Washington, District of Columbia, USA

Abstract Magnetic field observations acquired in orbit about Mercury by the MESSENGER spacecraft demonstrate the presence in the planet's northern hemisphere of Birkeland currents that flow to low altitudes. Currents of density 10–30 nA/m^2 flow downward at dawn and upward at dusk. Total currents are typically 20–40 kA and exceed 200 kA during disturbed conditions. The current density and total current are two orders of magnitude lower than at Earth. An electric potential of ~30 kV from dayside magnetopause magnetic reconnection implies a net electrical conductance of ~1 S. A spherical-shell conductance model indicates closure of current radially through the low-conductivity layers near the surface and by lateral flow from dawn to dusk through more conductive material at depth.

1. Introduction

The dynamics of Mercury's magnetosphere reflect external conditions not found at other planets in our solar system with internal magnetic fields. The solar wind density is higher, and the interplanetary magnetic field (IMF) is stronger and more aligned to the Sun-planet line at Mercury than at 1 AU [*Slavin et al.*, 2007; *Korth et al.*, 2011a]. Mercury occupies a larger fraction of its magnetosphere than does Earth: the subsolar standoff altitude is 0.4 R_M, where R_M = 2440 km is Mercury's radius [cf. *Johnson et al.*, 2012; *Winslow et al.*, 2013], whereas at Earth the standoff altitude is ~10 planetary radii [cf. *Wang et al.*, 2013]. The absence of an ionosphere at Mercury implies that electrodynamic coupling of the magnetosphere and the planet differs from that at Earth [*Glassmeier*, 2000]. At Earth, electric currents flow along the magnetic field, transmitting stress between the magnetosphere and ionosphere [*Iijima and Potemra*, 1976]. These field-aligned or Birkeland currents close in the ionosphere [*Cowley*, 2000; *Richmond and Thayer*, 2000].

Birkeland currents at Mercury were first reported from Mariner 10 observations by *Slavin et al.* [1997] and are seen in magnetospheric simulations for models with surface conductance [*Janhunen and Kallio*, 2004; *Ip and Kopp*, 2004]. There are several mechanisms for current closure at Mercury. *Glassmeier* [1997] estimated the conductance of the planet at ~10 s timescales by integrating the material conductivity over the skin depth. Transient currents, treated as Alfvén waves, are reflected from the surface and do not require closure [*Lyatsky et al.*, 2010]. At longer timescales, the low conductance of the regolith inhibits closure near the surface [*Glassmeier*, 1997]. Neutral exospheric densities give negligible Pedersen conductance via ion-neutral collisions [cf. *Slavin et al.*, 2007]. A conductance as high as 0.1 S might result from charge transport via a chain of collisions with the regolith; such collisions create secondary emissions that in turn collide with the regolith, producing additional secondary emissions [*Cheng et al.*, 1987]. *Janhunen and Kallio* [2004] proposed that currents could close through the planet, radially through the low-conductance outer layers of the crust and upper mantle and laterally at depths where temperature and conductance are higher. We report the first observations of magnetic signatures of Birkeland currents over Mercury's northern hemisphere from the Magnetometer on the MErcury Surface, Space ENvironment, GEochemistry, and Ranging (MESSENGER) spacecraft [*Solomon et al.*, 2007].

2. Data and Processing

Observations with MESSENGER's Magnetometer [*Anderson et al.*, 2007] have been acquired from orbit about Mercury [*McAdams et al.*, 2012] since 23 March 2011. We used 1 s averages of data acquired within

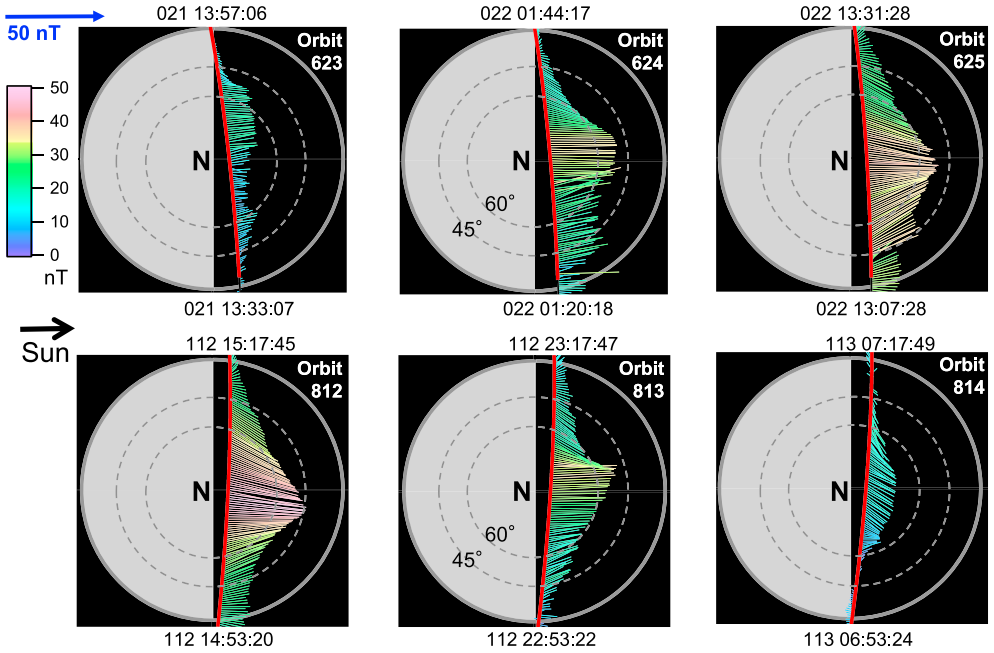

Figure 1. Magnetic perturbations recorded by MESSENGER as viewed from above Mercury's north pole during 21–22 January 2012 (upper panels) and 21–22 April 2012 (lower panels). The spacecraft trajectory is shown in red below 1000 km altitude. Magnetic residuals perpendicular to the total model field and projected onto the *X-Y* plane, $\delta\mathbf{B}_{XY}$, are plotted at 12 s intervals and shown by colored lines originating at the observation point. The directions correspond to the $\delta\mathbf{B}_{XY}$ direction, and the color and length indicate $|\delta\mathbf{B}_{XY}|$ (see color bar at left). Start and end times are given by day of year and UTC.

the magnetosphere. Complete coverage in local time is provided every 88 days. Magnetic field and spacecraft position data were processed in Mercury solar orbital (MSO) coordinates aberrated for Mercury's orbital motion [cf. *Johnson et al.*, 2012]. The MSO origin is the center of Mercury, and the *Z* axis is parallel to the planetary rotation axis, positive northward. Positive *X* is opposite to the solar wind flow in Mercury's frame, and the *Y* axis completes a right-handed system. Spacecraft position and measured magnetic field in this system are denoted $\mathbf{r}_{SC} = (X_{SC}, Y_{SC}, Z_{SC})$ and $\mathbf{B} = (B_X, B_Y, B_Z)$, respectively.

To resolve Birkeland current signatures, we subtracted model fields from the measurements. The internally generated magnetic field, $\mathbf{B}_{Int}$, was taken as a spin-axis-aligned, southward dipole of moment 190 nT R_M^3, offset 479 km northward along the spin axis [*Johnson et al.*, 2012; *Anderson et al.*, 2011, 2012]. The field of magnetopause and magnetotail currents, $\mathbf{B}_{Ext}$, was given by the external field model of *Johnson et al.* [2012]. To account for the variation of solar wind ram pressure with Mercury true anomaly, the subsolar magnetopause distance, R_{SS}, was taken to vary with heliocentric distance, r_M, as $R_{SS} = R_{SS0}(r_{M0}/r_M)^{1/3}$, where $R_{SS0} = 1.45\ R_M$ and $r_{M0} = 0.39$ AU [cf. *Korth et al.*, 2012]. The total model field, $\mathbf{B}_M(\mathbf{r},t) = \mathbf{B}_{Int}(\mathbf{r}) + \mathbf{B}_{Ext}(\mathbf{r},t)$, was subtracted from $\mathbf{B}$ to yield

$$\delta\mathbf{B} = \mathbf{B} - \mathbf{B}_M(\mathbf{r},t). \tag{1}$$

Variations in the solar wind pressure other than the mean variation with Mercury heliocentric distance are not included in $\mathbf{B}_{Ext}$. Variations in these currents not included in the mean model will be present in $\delta\mathbf{B}$, but these currents are distant from the spacecraft in all of the data analyzed here and are therefore curl free, so they do not contribute to the current density estimates described below.

The $\delta\mathbf{B}$ residuals contain cusp and plasma sheet diamagnetic depressions [*Winslow et al.*, 2012; *Korth et al.*, 2011b, 2012]. To exclude these signals, we subtracted the residual parallel to the total model field. From

$$\mathbf{b}_M = \mathbf{B}_M(\mathbf{r},t)/|\mathbf{B}_M(\mathbf{r},t)|\ , \tag{2}$$

the perpendicular residual is

$$\delta\mathbf{B}_\perp = \delta\mathbf{B} - (\delta\mathbf{B}\cdot\mathbf{b}_M)\mathbf{b}_M. \tag{3}$$

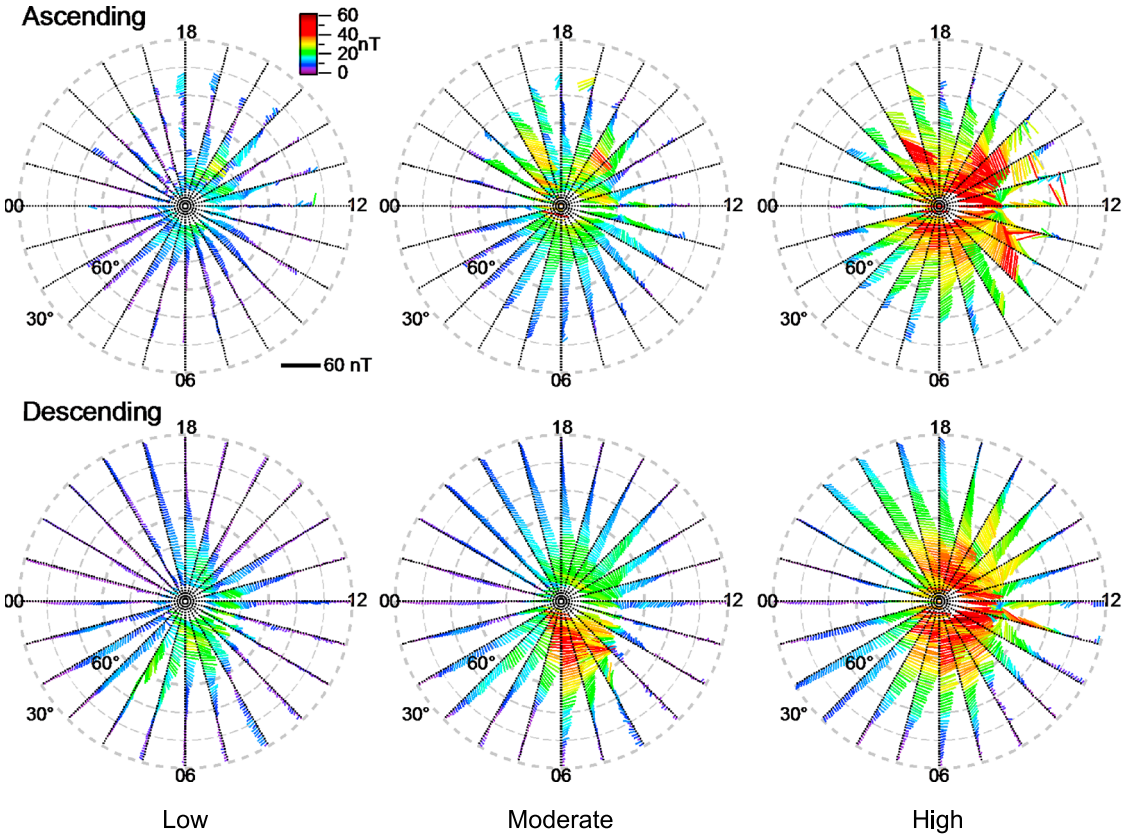

Figure 2. Average magnetic perturbations above Mercury's northern hemisphere in aberrated MSO coordinates during ascending (top) and descending (bottom) tracks for three levels of Mercury magnetic disturbance: 0–33% (left); 33–67% (center); and 67–100% (right). Averaged horizontal perturbations are plotted as lines from the bin center in the direction of the averaged vector. Line lengths and colors show the magnitude (see color bar at upper left). Gray dashed circles are spaced 10° in latitude.

Residuals were evaluated between the innermost magnetopause encounters [*Winslow et al.*, 2013] for data from 23 March 2011 to 28 April 2012.

3. Signatures of Birkeland Currents

Data for two sets of three successive orbits are shown in Figure 1. The residuals are projected onto the MSO *X-Y* plane and are displayed along the spacecraft trajectory in the northern hemisphere. The orbit sets are 90 days apart, so Mercury's subsolar longitude is oppositely directed in local time between the series. The largest residuals are primarily in the +*X* direction and poleward of λ ~60°N, where λ is MSO latitude given by asin(Z_{SC}/r_{SC}). The $\mathbf{\delta B}_\perp$ magnitude ($\delta B_\perp$) varies between passes. The consistently sunward direction of $\mathbf{\delta B}_\perp$ and the variability in $\delta B_\perp$ between passes imply that these signals are of external origin. Moreover, the $\mathbf{\delta B}_\perp$ vectors for a given pass over the polar region are smoothly varying, implying that their source mechanism is quasi-steady on the ~10 min time scale of these passes.

The perturbations indicate a sunward tilt of the radially inward magnetic field, consistent with magnetic convection. The mechanism for the tilt is a current flowing downward in the morning and upward in the evening, analogous to the Region 1 (R1) Birkeland currents at Earth [*Iijima and Potemra*, 1976]. At Earth, these currents increase with the solar wind electric field [e.g., *Korth et al.*, 2010] and are a signature of magnetospheric circulation [cf. *Cowley*, 2000]. The signatures in Figure 1 differ from those at Earth in two ways. First, only the sunward perturbation is evident, whereas at Earth the largest signal is located between the poleward R1 and equatorward Region 2 (R2) currents of opposite polarity and is anti-sunward in the north. Second, at Mercury, the signal is ~50 nT, whereas at Earth it is typically 500–1000 nT.

Average $\mathbf{\delta B}_\perp$ and current density maps were determined as follows. Each magnetosphere pass was ranked by the disturbance level of the magnetic field [*Anderson et al.*, 2013] in three ranges: low (0–33%), moderate

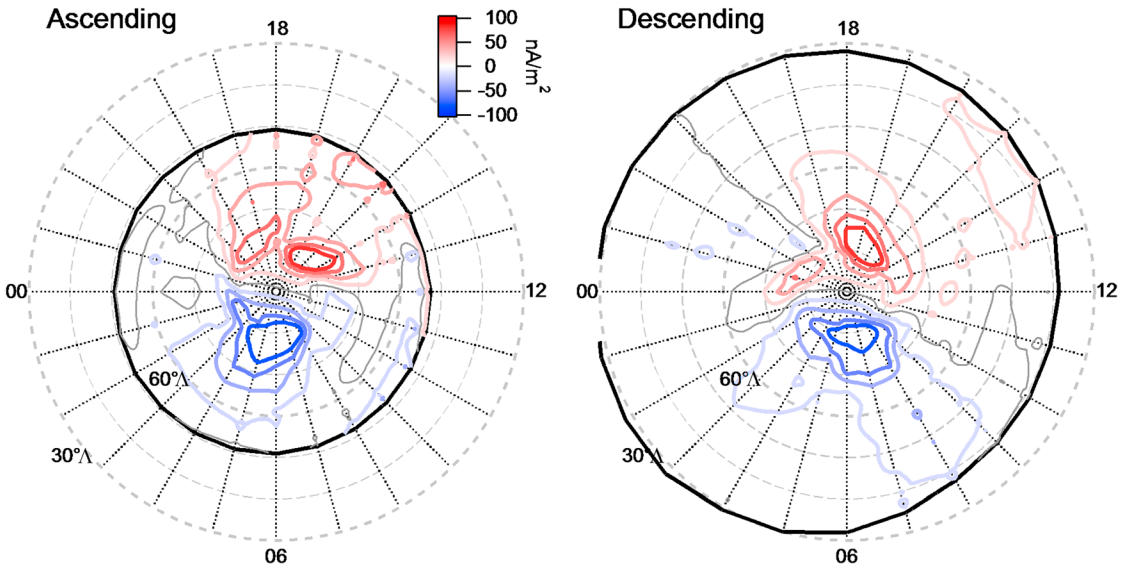

Figure 3. Contour plots of radial current density, J_{rS}, at Mercury's surface displayed versus local time in hours and invariant latitude, Λ. Left (right) panel shows results for the ascending (descending) track data. Heavy black line shows the equatorward boundary of the region over which J_{rS} was evaluated. Red and blue contours show upward and downward current, respectively, shaded by intensity as indicated by the color scale and plotted at 20 nA/m^2 intervals. Maximum and minimum J_{rS} are ±115 nA/m^2 for the ascending and ±83 nA/m^2 for the descending track data. The thin gray line shows the $J_{rS} = 0$ contour.

(33–67%), and high (67–100%). Data from orbit segments ascending ($d\lambda/dt > 0$) and descending ($d\lambda/dt < 0$) with latitude were analyzed separately, and only data from altitudes below 1000 km and northward of 30°N were retained. Data were binned by spacecraft position, aberrated MSO local time, and latitude. All $\delta\mathbf{B}_\perp$ vectors for each disturbance level within each bin, 1° in latitude by 1 h in local time, were averaged together.

Averaged residuals for each disturbance level are shown in Figure 2. For ascending and descending subsets and all activity levels, the perturbations are consistently sunward poleward of 60°N, where the amplitudes are also generally greatest. Near noon from 50°N to 70°N on the dayside, the residuals turn toward the noon-midnight meridian. The residual magnitudes increase with increasing disturbance level. The longest period used to derive the disturbance index is 300 s [*Anderson et al.*, 2013], shorter than the ~24 min interval during which signals were observed, implying that this correlation is not an artifact of the analysis.

The averages exhibit a dawn-dusk asymmetry. For all activity levels, the ascending orbit segment data have larger $\delta B_\perp$ at dusk than at dawn, whereas the opposite holds for the descending orbit segment data. Mercury perihelion occurs when MESSENGER's ascending orbit node is near dusk and the descending node is near dawn, so the solar wind density is highest and the IMF strongest when the ascending (descending) orbit leg is at dusk (dawn). We therefore expect the intensity of solar wind forcing to be highest in the ascending orbit leg data at dusk and in the descending orbit leg data at dawn. Mercury's plasma sheet pressure and magnetic variability both maximize at Mercury perihelion [*Anderson et al.*, 2013; *Korth et al.*, 2014]. We attribute the dawn-dusk asymmetries in the $\delta\mathbf{B}_\perp$ to higher magnetospheric activity at Mercury perihelion than at aphelion.

4. Current Derivation and Closure

The magnetic perturbations imply currents, which we quantified using Ampere's law, $\nabla \times \delta\mathbf{B}_\perp = \mu_0 J_r \mathbf{n}_r$, where μ_0 is the magnetic permeability of free space, J_r is the radial current density, and $\mathbf{n}_r$ is the radial unit vector. The current was estimated by integrating $0.5(\delta\mathbf{B}_{\perp k} + \delta\mathbf{B}_{\perp l}) \cdot \mathbf{ds}_{kl}$ around each grid cell intersection, where $\delta\mathbf{B}_{\perp k}$ and $\delta\mathbf{B}_{\perp l}$ are the average $\delta\mathbf{B}_\perp$ for the kth and lth grid cells, and $\mathbf{ds}_{kl}$ is the path element from the lth to kth grid center. At the minimum latitude boundary, the $\delta\mathbf{B}_\perp$ at each local time was interpolated from the minimum latitude with observations to 0 nT at the equator. The perturbation at the pole was assigned the local time-averaged $\delta\mathbf{B}_\perp$ at the maximum latitude, 83°N. At each local time, the $\delta\mathbf{B}_\perp$ value was interpolated from 83°N to this value at the pole. The current divided by the cell area gives J_r, which was smoothed with a moving average over 5° latitude by 3 h.

Table 1. Integrated Birkeland Current in the Dawn and Dusk Sectors for Ascending and Descending Orbit Data Versus Magnetic Disturbance Level

	Integrated Birkeland Current (kA)				
	Ascending		Descending		
Magnetic Disturbance Level	01–11 h	13–23 h	01–11 h	13–23 h	Average Abs. Value
Low (0–33%)	−18.4	18.2	−21.1	14.0	17.9
Moderate (33–67%)	−24.9	33.2	−30.8	20.2	27.3
High (67–100%)	−38.4	41.8	−38.3	33.5	38.0
All	−32.9	35.8	−33.7	26.4	32.2

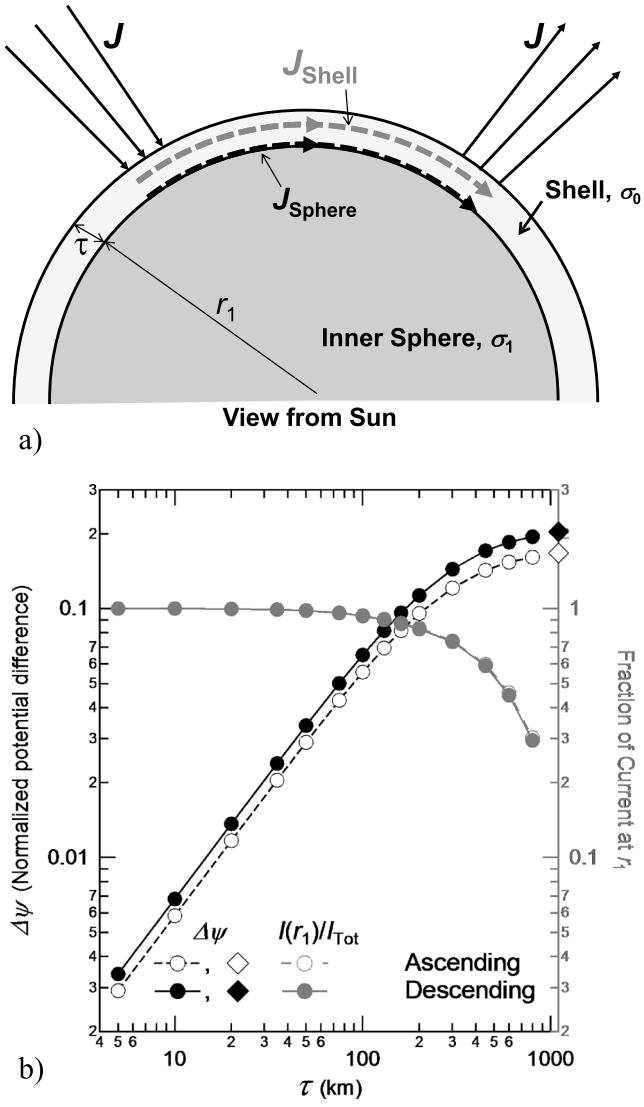

Figure 4. (a) Conductivity model used to derive the electric potential implied by J_{rS}, and (b) maximum normalized potential difference, $\Delta\psi$, shown in black symbols and scaled on the left axis, and fraction of total radial current at the inner surface to the total current, $I(r_1)/I_{Tot}$, shown in gray symbols and scaled on the right axis, from solutions to Laplace's equation versus shell thickness, τ. Results are shown using J_{rS} from both the ascending (open symbols) and descending (closed symbols) orbit segment data.

The current density at the surface, J_{rS}, was calculated by multiplying J_r by the ratio of the cell area at spacecraft altitude to the cell area projected along $\mathbf{B}_M$ to the surface foot point in the northern hemisphere. The J_{rS} values are displayed versus invariant latitude, Λ, in Figure 3, where invariant latitude is given by the intersection of a magnetic field line threading the observation point with a sphere of radius R_M centered at the offset dipole [cf. *Korth et al*., 2014]. For ascending and descending tracks, the current is downward in the dawn sector and upward in the evening sector, like R1 currents at Earth. Although currents extend to $\Lambda \sim 50°$, the highest current densities are from $\Lambda = 70°$ to 80°. The descending orbit data extend ~20° equatorward of the primary current regions without evidence of opposite-polarity R2 currents.

The total currents for each magnetic disturbance range (Table 1) were calculated by summing the current poleward of 60°N ($\Lambda = 58°$ ascending, $\Lambda = 53°$ descending) in two local time ranges, 01 to 11 h and 13 to 23 h. The increase in total current with disturbance is a factor of ~2, and the average current is ~30 kA. Opposite dawn-dusk asymmetries in the ascending and descending orbit segment data are generally evident. (The disturbance index is independent of the Mercury-Sun distance [*Anderson et al*., 2013].) The electric potential applied to Mercury's magnetosphere via dayside magnetic reconnection is ~30 kV [*Slavin et al*., 2009, 2012; *DiBraccio et al*., 2013], given nominal

values for reconnection line length and magnetosheath flow speed, so the effective electrical conductance is ~1 S. This value is too high for either Pedersen conductance in the exosphere or regolith charge transport [*Cheng et al.*, 1987; *Slavin et al.*, 2007], so we consider current closure within the planet [*Janhunen and Kallio*, 2004].

The potential difference implied by the current distributions was determined with the model illustrated in Figure 4a. The model consists of an outer shell of thickness τ and conductivity σ_0, and an inner sphere of radius r_1 and conductivity σ_1. Because mineral conductivity increases strongly with temperature and hence with depth [*Breuer et al.*, 2007], we set $\sigma_1 = \infty$ and solved Laplace's equation, $\nabla^2\varphi = 0$, for the electrical potential, φ, subject to the boundary conditions

$$-\left.\frac{\partial\varphi}{\partial r}\right|_{r=R_M} = \frac{J_{rS}}{\sigma_0} \tag{4a}$$

$$\varphi|_{r=r_1} = 0 \tag{4b}$$

where equation (4a) is the electric field just inside the surface and equation (4b) corresponds to a constant potential at $r = r_1$, set equal to zero. We used the J_{rS} values with surface magnetic foot points poleward of 60°N, equivalent to $\Lambda > 50°$. When solving for the potential, we ignored the currents in the southern hemisphere by taking $J_{rS} = 0$ everywhere south of 60°N, an approximation we test below. We calculated the normalized potential, ψ, defined by $\psi = \varphi\sigma_0/(R_M J_{rS,max})$, where $J_{rS,max}$ is the largest value of $|J_{rS}|$. Results are shown in Figure 4b for the maximum potential difference, i.e., the difference between the maximum and minimum normalized potential, $\Delta\psi = \psi_{Max} - \psi_{Min}$, and the fraction of current closing in the inner sphere, $I(r_1)/I_{Tot}$, versus τ for spherical harmonic solutions to degree and order 24, consistent with the 1 h local time binning in J_{rS}. To test the validity of setting $J_{rS} = 0$ in the south, we calculated the maximum potential difference at 45°N, $\Delta\psi_{45}$. For $\tau < 420$ km, corresponding to the best estimate for the depth to the top of the fluid outer core [*Hauck et al.*, 2013], we found $\Delta\psi_{45}/\Delta\psi < 0.02$, confirming that the potential is confined to latitudes poleward of 45°N. This result also implies that any currents of Region 2 polarity are at most a few percent of the observed currents. The solutions for ascending and descending track data differ in the ψ scaling factor because $J_{rS,max}$ is ~20% higher for the ascending track results. The three-standard-deviation standard error in φ is 13 kV [cf. Figure 12 of *DiBraccio et al.*, 2013].

These results for the shell model imply that the current closes radially through the shell and laterally via the inner sphere. The conductivity should increase by up to ~6 orders of magnitude from the surface to 150 km depth [cf. *Breuer et al.*, 2007; *Verhoeven et al.*, 2009; *Williams et al.*, 2011], so we expect that the thin-shell regime is the most applicable. For $\tau < 150$ km, we find that $I(r_1)/I_{Tot} > 0.9$ and $\Delta\psi$ is proportional to τ, as expected if the potential is dominated by the resistive drop through the shell. The ratio, $\tau/\Delta\psi$, is 1.6×10^3 km at $\tau = 5$ km and is 9% higher at $\tau = 130$ km.

For this current closure path, we can relate the shell model to a more general conductivity-depth profile. If we approximate the thin shell ($\tau << r_1$) by a horizontal slab of thickness τ, horizontal cross-sectional area A, and conductivity $\sigma(x)$ as a function of depth, x, then the resistance is

$$\rho = \frac{1}{A}\int_0^\tau \frac{dx}{\sigma(x)}. \tag{5}$$

Note that A is arbitrary since we are interested only in comparing the depth integral for different $\sigma(x)$. For the shell model, σ is constant (σ_0) so the effective resistance is proportional to $\tau/\Delta\psi$. With $\sigma(x) = \sigma_s \exp(bx)$, where σ_s is the near-surface conductivity and $1/b$ is the e-folding depth [e.g., *Constable*, 2006; *Verhoeven et al.*, 2009], we obtain

$$\rho = \frac{1}{A}\frac{1}{\sigma_s b}[1 - \exp(-b\tau)]. \tag{6}$$

The conductivity-depth profiles of *Verhoeven et al.* [2009] have an e-folding depth for $\sigma(x)$ near 5 km for depths up to ~100 km. Thus, for τ ~50 to 100 km, $b\tau >> 1$ and $\exp(-b\tau)$ is negligible. Equating ρ from the shell model to that from the conductivity-depth profiles of *Verhoeven et al.* [2009] gives

$$\frac{\tau}{\sigma_0} = \frac{1}{\sigma_s b}. \tag{7}$$

From $\Delta\psi = \varphi\sigma_0/(R_M J_{rS,max})$, we obtain

$$\sigma_s = \frac{1}{b}\left(\frac{\Delta\psi}{\tau}\right)\left(\frac{R_M J_{rS,max}}{\varphi}\right), \quad (8)$$

and since $\Delta\psi/\tau$ is constant, σ_s ~$2.5 \pm 1.2 \times 10^{-8}$ S/m, where the uncertainty is dominated by that in φ. The quantity $\sigma_s b$ ~$5.0 \pm 2.4 \times 10^{-11}$ S/m^2 provides a constraint on conductance models with different depth scaling.

5. Discussion and Conclusions

MESSENGER magnetic field observations of Birkeland currents at Mercury suggest that the currents close through the planet, flowing radially through the lower-conductivity upper crust and laterally at depth, where the conductivity should be substantially higher. Semi-empirical models for dry olivine [*Constable*, 2006] yield σ ~10^{-6} S/m at ~900 K and $\sigma > 10^{-2}$ S/m at 2000 K. Conductivity estimates for different models of the composition of Mercury's crust and mantle and two thermal evolution models [*Verhoeven et al*., 2009] give conductivities from 10^{-3} to as much as 1 S/m at depths of 350 to 420 km, relevant to Mercury's lowermost mantle [*Hauck et al*., 2013]. *Verhoeven et al*. estimated crustal conductivities for volcanic rocks formed from magmas having compositions consistent with their model mantle mineralogies and found σ ~10^{-6} S/m at 100 km and ~10^{-11} S/m near the surface for all models except the metal-rich chondrite model of *Taylor and Scott* [2005], for which σ ~10^{-2} to 1 S/m from the surface to ~100 km depth. Our results rule out the metal-rich chondrite model, consistent with the low surface abundances of iron indicated by X-ray spectrometry [*Weider et al*., 2012]. Our estimate for σ_s is higher than in the models of *Verhoeven et al*. [2009], but those models were constructed before high abundances of sulfur were documented on Mercury's surface [*Weider et al*., 2012].

We note three aspects of these results. First, the total energy dissipated will be 30 kA at 30 kV or ~1 GW, which over the area poleward of 60°N amounts to a flux of only 0.2 mW/m^2. Second, the currents correspond to particle fluxes to the surface. Given that upward (downward) currents are carried by downward electrons (positive ions), a 30 kA current corresponds to a flux to the surface of 2×10^{23} electrons per second in the afternoon and the same flux of ions in the morning, but this particle flux is only ~20% of that to the northern cusp [*Winslow et al*., 2012]. Third, relatively smooth signatures on a given pass indicate that large-scale Birkeland currents are quasi-steady for time scales of at least ~10 min despite the short time scale for magnetospheric convection and even shorter time scale for reconnection signatures [*Slavin et al*., 2012; *DiBraccio et al*., 2013; *Imber et al*., 2014]. Although bursts in reconnection contribute to convection, the net effect is quasi-steady convection. The statistical results reflect time-averaged currents and not those associated with substorms or bursts of magnetic reconnection [e.g., *Slavin et al*., 1997, 2012].

The absence of R2-polarity currents is intriguing. It is unlikely that such currents are present, because the observations extend ~20° equatorward of the R1 currents without an indication of R2 patterns. At Earth, R2 currents occur within 10° latitude of R1 [cf. *He et al*., 2012]. The close proximity of the currents minimizes energy dissipation [e.g., *Barbosa*, 1988], and R2 currents close at high altitudes in the magnetosphere through gradients in plasma pressure and flow shears [e.g., *Brandt et al*., 2004]. If R2 currents are present at Mercury, they are located within ±30° invariant latitude of the magnetic equator, very close to the planet. It is unclear how the energetics would favor such a configuration.

Steady-state Birkeland currents at Mercury are different from those at Earth. The current densities are two orders of magnitude lower than current densities at Earth, 1–10 μA/m^2 [cf. *Richmond and Thayer*, 2000], and close through the planet. The absence of R2 currents may reflect a fundamental difference in magnetospheric convection from that at Earth. At Earth, convection flows return magnetic flux to the dayside, and the R2 currents are generated in the process. These flows extend within a geocentric distance of ~6 Earth radii. Relative to the planet, Mercury's magnetosphere is a factor of ~8 smaller than Earth's, so the source of R2 currents at Mercury would lie beneath the surface. Thus, plasma convecting sunward from the nightside magnetosphere may impact Mercury's surface before it produces R2 currents. The observations of Birkeland currents reported here therefore could have important implications for the configuration of magnetospheric return convection at Mercury.

Acknowledgments

We thank two reviewers for constructive comments on an earlier draft. The MESSENGER project is supported by the NASA Discovery Program under contracts NAS5-97271 to The Johns Hopkins University Applied Physics Laboratory and NASW-00002 to the Carnegie Institution of Washington. C. L. Johnson is supported by MESSENGER Participating Scientist grants NNX11AB84G and NNH08CC05C. R. M. Winslow and C. L. Johnson acknowledge support from the Natural Sciences and Engineering Research Council of Canada. MESSENGER data are available from the Planetary Data System (https://pds.jpl.nasa.gov).

Andrew Dombard thanks two anonymous reviewers for their assistance in evaluating this paper.

References

Anderson, B. J., M. H. Acuña, D. A. Lohr, J. Scheifele, A. Raval, H. Korth, and J. A. Slavin (2007), The Magnetometer instrument on MESSENGER, *Space Sci. Rev.*, *131*, 417–450, doi:10.1007/s11214-007-9246-7.

Anderson, B. J., C. L. Johnson, H. Korth, M. E. Purucker, R. M. Winslow, J. A. Slavin, S. C. Solomon, R. L. McNutt Jr., J. M. Raines, and T. H. Zurbuchen (2011), The global magnetic field of Mercury from MESSENGER orbital observations, *Science*, *333*, 1859–1862, doi:10.1126/science.1211001.

Anderson, B. J., C. L. Johnson, H. Korth, R. M. Winslow, J. E. Borovsky, M. E. Purucker, J. A. Slavin, S. C. Solomon, M. T. Zuber, and R. L. McNutt Jr. (2012), Low-degree structure in Mercury's planetary magnetic field, *J. Geophys. Res.*, *117*, E00l12, doi:10.1029/2012JE004159.

Anderson, B. J., C. L. Johnson, and H. Korth (2013), A magnetic disturbance index for Mercury's magnetic field derived from MESSENGER Magnetometer data, *Geochem. Geophys. Geosyst.*, *14*, 3875–3886, doi:10.1002/ggge.20242.

Barbosa, D. D. (1988), Minimal joule dissipation models of magnetospheric convection, *Pure Appl. Geophys.*, *127*, 473–489, doi:10.1007/BF00879822.

Brandt, P. C.:s., E. C. Roelof, S. Ohtani, D. G. Mitchell, and B. Anderson (2004), IMAGE/HENA: Pressure and current distributions during the 1 October 2002 storm, *Adv. Space Res.*, *33*, 719–722, doi:10.1016/S0273-1177(03)00633-1.

Breuer, D., S. A. Hauck II, M. Buske, M. Pauer, and T. Spohn (2007), Interior evolution of Mercury, *Space Sci. Rev.*, *132*, 229–260, doi:10.1007/s11214-007-9228-9.

Cheng, A. F., R. E. Johnson, S. M. Krimigis, and L. J. Lanzerotti (1987), Magnetosphere, exosphere, and surface of Mercury, *Icarus*, *71*, 430–440, doi:10.1016/0019-1035(87)90038-8.

Constable, S. (2006), SEO3: A new model of olivine electrical conductivity, *Geophys. J. Int.*, *166*, 435–437, doi:10.1111/j.1365-246X.2006.03041.x.

Cowley, S. W. H. (2000), Magnetosphere-ionosphere interactions: A tutorial review, in *Magnetospheric Current Systems*, *Geophys. Monogr. Ser.*, vol. 118, edited by S. Ohtani, R. Fujii, M. Hesse, and R. L. Lysak, pp. 91–106, AGU, Washington, D. C., doi:10.1029/GM118p0091.

DiBraccio, G. A., J. A. Slavin, S. A. Boardsen, B. J. Anderson, H. Korth, T. H. Zurbuchen, J. M. Raines, D. N. Baker, R. L. McNutt Jr., and S. C. Solomon (2013), MESSENGER observations of magnetopause structure and dynamics at Mercury, *J. Geophys. Res. Space Physics*, *118*, 997–1008, doi:10.1029/2012JA017959.

Glassmeier, K. H. (2000), Currents in Mercury's magnetosphere, in *Magnetospheric Current Systems*, *Geophys. Monogr. Ser.*, vol. 118, edited by S.-I. Ohtani, R. Fujii, M. Hesse, and R. L. Lysak, pp. 371–380, AGU, Washington, D. C., doi:10.1029/GM118p0371.

Glassmeier, K.-H. (1997), The Hermean magnetosphere and its ionosphere–magnetosphere coupling, *Planet. Space Sci.*, *45*, 119–125.

Hauck, S. A., II, et al. (2013), The curious case of Mercury's internal structure, *J. Geophys. Res. Planets*, *118*, 1204–1220, doi:10.1002/jgre.20091.

He, M., J. Vogt, H. Lühr, E. Sorbalo, A. Blagau, G. Le, and G. Lu (2012), A high-resolution model of field-aligned currents through empirical orthogonal functions analysis (MFACE), *Geophys. Res. Lett.*, *39*, L18105, doi:10.1029/2012GL053168.

Iijima, T., and T. A. Potemra (1976), The amplitude distribution of field-aligned currents at northern high latitudes observed by Triad, *J. Geophys. Res.*, *81*, 2165–2174, doi:10.1029/JA081i013p02165.

Imber, S. M., J. A. Slavin, S. A. Boardsen, B. J. Anderson, H. Korth, R. L. Mcnutt Jr., and S. C. Solomon (2014), MESSENGER observations of large dayside flux transfer events: Do they drive Mercury's substorm cycle?, *J. Geophys. Res. Space Physics*, *119*, 5613–5623, doi:10.1002/2014JA019884.

Ip, W.-H., and A. Kopp (2004), Mercury's Birkeland current system, *Adv. Space Res.*, *33*, 2171–2175, doi:10.1016/S0273-1177(03)00444-7.

Janhunen, P., and E. Kallio (2004), Surface conductivity of Mercury provides current closure and may affect magnetospheric symmetry, *Ann. Geophys.*, *22*, 1829–1837, doi:10.5194/angeo-22-1829-2004.

Johnson, C. L., et al. (2012), MESSENGER observations of Mercury's magnetic field structure, *J. Geophys. Res.*, *117*, E00l14, doi:10.1029/2012JE004.

Korth, H., B. J. Anderson, and C. L. Waters (2010), Statistical analysis of the dependence of large-scale Birkeland currents on solar wind parameters, *Ann. Geophys.*, *28*, 515–530.

Korth, H., B. J. Anderson, T. H. Zurbuchen, J. A. Slavin, S. Perri, S. A. Boardsen, D. N. Baker, S. C. Solomon, and R. L. McNutt Jr. (2011a), The interplanetary magnetic field environment at Mercury's orbit, *Planet. Space Sci.*, *59*, 2075–2085, doi:10.1016/j.pss.2010.10.014.

Korth, H., B. J. Anderson, J. M. Raines, J. A. Slavin, T. H. Zurbuchen, C. L. Johnson, M. E. Purucker, R. M. Winslow, S. C. Solomon, and R. L. McNutt Jr. (2011b), Plasma pressure in Mercury's equatorial magnetosphere derived from MESSENGER Magnetometer observations, *Geophys. Res. Lett.*, *38*, L22201, doi:10.1029/2011GL049451.

Korth, H., B. J. Anderson, C. L. Johnson, R. M. Winslow, J. A. Slavin, M. E. Purucker, S. C. Solomon, and R. L. McNutt Jr. (2012), Characteristics of the plasma distribution in Mercury's equatorial magnetosphere derived from MESSENGER Magnetometer observations, *J. Geophys. Res.*, *117*, A00M07, doi:10.1029/2012JA018052.

Korth, H., B. J. Anderson, D. J. Gershman, J. M. Raines, J. A. Slavin, T. H. Zurbuchen, S. C. Solomon, and R. L. McNutt Jr. (2014), Plasma distribution in Mercury's magnetosphere derived from MESSENGER magnetometer and fast imaging plasma spectrometer observations, *J. Geophys. Res. Space Physics*, *119*, 2917–2932, doi:10.1002/2013JA019567.

Lyatsky, W., G. V. Khazanov, and J. A. Slavin (2010), Alfvén wave reflection model of field-aligned currents at Mercury, *Icarus*, *209*, 40–45, doi:10.1016/j.icarus.2009.11.039.

McAdams, J. V., et al. (2012), MESSENGER at Mercury: From orbit insertion to first extended mission, *63rd International Astronautical Congress*, paper IAC-12-C1.5.6, 11 pp., Naples, Italy, 1–5 Oct.

Richmond, A. D., and J. P. Thayer (2000), Ionospheric dynamics: A tutorial, in *Magnetospheric Current Systems*, *Geophys. Monogr. Ser.*, vol. 118, edited by S. Ohtani, R. Fujii, M. Hesse, and R. L. Lysak, pp. 131–146, AGU, Washington, D. C., doi:10.1029/GM118p0131.

Slavin, J. A., J. C. J. Owen, J. E. P. Connerney, and S. P. Christon (1997), Mariner 10 observations of field-aligned currents at Mercury, *Planet. Space Sci.*, *45*, 133–141.

Slavin, J. A., et al. (2007), MESSENGER: Exploring Mercury's magnetosphere, *Space Sci. Rev.*, *131*, 133–160.

Slavin, J. A., et al. (2009), MESSENGER observations of magnetic reconnection in Mercury's magnetosphere, *Science*, *324*, 606–610, doi:10.1126/science.1172011.

Slavin, J. A., et al. (2012), MESSENGER observations of a flux-transfer-event shower at Mercury, *J. Geophys. Res.*, *117*, A00M06, doi:10.1029/2012JA017926.

Solomon, S. C., R. L. McNutt Jr., R. E. Gold, and D. L. Domingue (2007), MESSENGER mission overview, *Space Sci. Rev.*, *131*, 3–39, doi:10.1007/s11214-007-9247-6.

Taylor, G. I., and E. R. F. Scott (2005), Mercury, in *Meteorites, Comets, and Planets*, *Treatise on Geochemistry*, 2nd ed., vol. 1, edited by A. M. Davis, pp. 477–485, Elsevier, Amsterdam.

Verhoeven, O., P. Tarits, P. Vacher, A. Rivoldini, and T. Van Hoolst (2009), Composition and formation of Mercury: Constraints from future electrical conductivity measurements, *Planet. Space Sci.*, *57*, 296–305, doi:10.1016/j.pss.2008.11.015.

Wang, Y., D. G. Sibeck, J. Merka, S. A. Boardsen, H. Karimabadi, T. B. Sipes, J. Šafránková, K. Jelínek, and R. Lin (2013), A new three-dimensional magnetopause model with support vector regression machine and a large database of multiple spacecraft observations, *J. Geophys. Res. Space Physics*, *118*, 2173–2184, doi:10.1002/jgra.50226.

Weider, S. Z., L. R. Nittler, R. D. Starr, T. J. McCoy, K. R. Stockstill-Cahill, P. K. Byrne, B. W. Denevi, J. W. Head, and S. C. Solomon (2012), Chemical heterogeneity on Mercury's surface revealed by the MESSENGER X-Ray Spectrometer, *J. Geophys. Res.*, *117*, E00L05, doi:10.1029/2012JE004153.

Williams, J.-P., J. Ruiz, M. A. Rosenburg, O. Aharonson, and R. J. Phillips (2011), Insolation driven variations of Mercury's lithospheric strength, *J. Geophys. Res.*, *116*, E01008, doi:10.1029/2010JE003655.

Winslow, R. M., C. L. Johnson, B. J. Anderson, H. Korth, J. A. Slavin, M. E. Purucker, and S. C. Solomon (2012), Observations of Mercury's northern cusp region with MESSENGER's Magnetometer, *Geophys. Res. Lett.*, *39*, doi:10.1029/2012GL051472.

Winslow, R. M., B. J. Anderson, C. L. Johnson, J. A. Slavin, H. Korth, M. E. Purucker, D. N. Baker, and S. C. Solomon (2013), Mercury's magnetopause and bow shock from MESSENGER Magnetometer observations, *J. Geophys. Res. Space Physics*, *118*, 2213–2227, doi:10.1002/jgra.50237.